ELSEVIER

NeuroImage

www.elsevier.com/locate/ynimg
NeuroImage 39 (2008) 1549–1558

Novel three-dimensional analysis tool for vascular trees indicates complete micro-networks, not single capillaries, as the angiogenic endpoint in mice overexpressing *human* $VEGF_{165}$ in the brain

Stefan Heinzer,[a,1] Gisela Kuhn,[b,1] Thomas Krucker,[c] Eric Meyer,[d] Alexandra Ulmann-Schuler,[d] Marco Stampanoni,[e] Max Gassmann,[b] Hugo H. Marti,[f] Ralph Müller,[a] and Johannes Vogel[b,*]

[a]*Institute for Biomedical Engineering, University and ETH Zürich, Zürich, Switzerland*
[b]*Institute of Veterinary Physiology and Zürich Center for Integrative Human Physiology (ZIHP), University of Zürich, Zürich, Switzerland*
[c]*Discovery Technologies, Novartis Institutes for BioMedical Research (NIBRI), Cambridge, MA, USA*
[d]*Institute of Zoology, University of Zürich, Zürich, Switzerland*
[e]*Swiss Light Source, Paul Scherrer Institut, Villigen, Switzerland*
[f]*Department of Physiology and Pathophysiology, University of Heidelberg, Heidelberg, Germany*

Received 27 July 2007; revised 20 October 2007; accepted 31 October 2007
Available online 12 November 2007

To adequately supply tissues with oxygen and nutrients, the formation of functional vascular networks requires generation of normal, healthy vessels and their arrangement into an effective network architecture. While our knowledge about the development of single vessels significantly increased during the last years, mechanisms responsible for network formation are still poorly understood. This is probably due to the lack of suitable methods for quantification of structural properties of microvascular networks.

Previously we showed that cerebral blood flow is not increased in mice exhibiting a 2- to 3-fold higher density of normal and perfused capillaries as a result of transgenic overexpression of the *human* vascular endothelial growth factor ($VEGF_{165}$). Here we used vascular corrosion casting and hierarchical micro-computed tomography combined with a new network analysis tool to characterize the vascular architecture in gray and white matter of these mice. Our results indicate that VEGF overexpression leads to formation of additional micro-networks connected to higher order vessels rather than insertion of individual capillaries into the existing vessel structure. This implies that the smallest "angiogenic quantum", i.e. the final, stable result of angiogenesis and subsequent remodeling, is not a single microvessel, but a complete micro-network. In conclusion, high-resolution 3D imaging combined with network analysis can substantially improve our understanding of vascular architecture, beneficial for the development of therapeutic angiogenesis as a clinical tool for applications such as wound healing or treatment of ischemic diseases.

Keywords: Vascular endothelial growth factor; Micro-computed tomography; Vascular remodeling; Network analysis; Morphometry

Introduction

One of the key players in the development of blood vessels is the vascular endothelial growth factor (VEGF). Increased VEGF expression leads to increased segment density of capillary networks (Marti et al., 2000; Ment et al., 1997; Pettersson et al., 2000) and has been used to induce vessel growth in ischemic diseases (Hayashi et al., 1998; Isner et al., 1996a,b). However, locally elevated VEGF levels induced by injection or viral transfection resulted in formation of abnormal, leaky vessels (Carmeliet and Jain, 2000; Vogel et al., 2003), suggesting that additional cytokines are mandatory for the development of fully functional vessel networks. Since brain-specific overexpression of *human* $VEGF_{165}$ in mice led to growth of normal, functional vessels (Vogel et al., 2004) such additional factors seem to be activated in these animals. Interestingly, cerebral blood flow was only marginally increased, despite up to 3-fold higher capillary density in *transgenic (tg) animals* (Vogel et al., 2004) indicating that the vascular network was built in an ineffective manner. Thus, besides dynamic blood flow regulation through changes in arteriolar diameter (Iadecola, 2004), the architecture of the vascular network is of utmost importance to ensure sufficient supply of the tissues with nutrients and oxygen.

* Corresponding author. Institute of Veterinary Physiology, Vetsuisse Faculty University of Zürich, Winterthurerstr. 260, CH-8057 Zürich, Switzerland. Fax: +41 44 6358932.
E-mail address: ogel@vetphys.uzh.ch (J. Vogel).
[1] These authors contributed equally.
Available online on ScienceDirect (www.sciencedirect.com).

1053-8119/$ - see front matter © 2007 Elsevier Inc. All rights reserved.
doi:10.1016/j.neuroimage.2007.10.054

Moreover, metabolic demand is not static throughout life resulting in continuous adaptation of the vasculature, a process known as vascular remodeling (Pries and Secomb, 2000; Pries et al., 1995a,b, 1998; Zakrzewicz et al., 2002). Such changes must affect not only the number of vessel segments, but also their 3-dimensional (3D) arrangement. So far it remains unclear which architectural parameters determine perfusion efficiency. A prerequisite to study the biology of vascular remodeling is therefore methods that enable imaging and quantification of 3D structural properties of vascular networks. A recently developed approach for this purpose is hierarchical microimaging based on vascular corrosion casting (VCC) in combination with multimodal micro-computed tomography (μCT) (Heinzer et al., 2006). Medium resolution μCT images (16 μm nominal voxel size) allow precise navigation within the VCCs to select regions of interest (ROI), which then are imaged non-destructively by synchrotron radiation μCT (SRμCT) at a resolution sufficient to visualize the capillary network (1.4 μm nominal voxel size). Resulting digital 3D datasets allow automated morphometric analysis of tissue volumes large enough for reliable statistical analysis (Heinzer et al., 2006).

Commercial software developed for morphometric analysis of cancellous bone has been used to quantify microvascular architecture (Heinzer et al., 2006). However, this software is not specific to important vascular properties since it treats the structure as a global entity, thereby lacking the concept of local elements (vessel bifurcations, vessel segments) and their hierarchical organization into functional levels and vessel trees. A possible solution is the transformation of voxel-based vessel images into a formal representation which can be analyzed by means of mathematical graph theory, also referred to as tree analysis (Bullitt et al., 2005; Palagyi and Kuba, 1998). Only little work is available treating classifications of large microvascular networks that include the capillary bed (Kassab, 2006). This is due to the fact that imaging modalities such as μCT and MRI could not resolve vessels with diameters below 20 μm (Dorr et al., 2007; Kiessling et al., 2004; Marxen et al., 2004).

In this paper we present a vessel network analysis method and its application to study 3D vessel morphology in mice overexpressing $VEGF_{165}$ in the brain. The method was designed to deal with large vascular networks as obtained from SRμCT imaging, which include the capillary network. Automatic extraction of vessel segments and computation of structural parameters were assessed with respect to correctness and computational efficiency. High-resolution 3D images from selected anatomical ROIs were acquired from $VEGF_{165}$ tg and wildtype (wt) control mice using the hierarchical imaging paradigm, based on VCC and SRμCT imaging. Our results indicate that VEGF overexpression leads to formation of complete additional micro-networks connected to higher order vessels rather than insertion of single capillaries into the existing network. New structural indices calculated from network analysis complement global morphometry and provide new insight in the complex vessel network organization.

Materials and methods

Sample preparation

All animal experiments conformed to institutional guidelines and were approved by the Kantonales Veterinäramt Zürich. Transgenic mice expressing brain-specific six-fold higher $VEGF_{165}$ levels (Vogel et al., 2004; Wang et al., 2005) and wt littermates (4–5 males of each line, age 16±2 weeks) were deeply anesthetized with 100 mg/kg pentobarbital (i.p.) and perfused through the left ventricle with 20 ml artificial cerebrospinal fluid containing 25,000 U/l heparin followed by 4% paraformaldehyde in phosphate buffered saline (PBS) and then by the new polymer resin PU4ii (vasQtec, Zürich, Switzerland) (Krucker et al., 2006) at 4 ml/min and 110 mm Hg. After resin curing, soft tissue was macerated in 7.5% KOH followed by decalcification of surrounding bone with 5% formic acid. The cerebral vasculature, including cerebellum and olfactory bulb, was dissected from the remaining extra cranial vessels, resulting in full brain casts with a size of about 16×10×8 mm. Casts were washed in distilled water and dried by lyophilization. In order to reach better absorption contrast in the X-ray scans, corrosion casts were stained using osmium tetroxide (Riew and Smith, 1971). Casts were mounted using cyano-acrylat glue on custom made Plexiglas stubs equipped with stainless steel pins for sample repositioning in the μCT (Heinzer et al., 2006).

Desktop μCT imaging and region of interest (ROI) selection

Three-dimensional images of whole brain samples were acquired using a desktop μCT system (μCT 40, Scanco Medical AG, Bassersdorf, Switzerland) operated at 50 kVp and 160 mA with a nominal isotropic voxel size of 16 μm. Per scan, 1000 projection images were acquired with an integration time of 200 ms and additional three times frame averaging for improved signal-to-noise ratio (SNR). Detailed information on the experimental setup is available elsewhere (Heinzer et al., 2006). Tomographic images were reconstructed, segmented, and imported into custom-made ROI picker software. For this study, one ROI of 1 mm^3 was placed in each of the following anatomical regions: corpus callosum (COCA), parietal cortex (CORT), forceps minor (FOMI), and hippocampus, close to the dentate gyrus (HIPC) (Fig. 1). Relative positions of ROIs with respect to the two pins in the sample holder were calculated and saved for subsequent measurement at the synchrotron beamline.

High-resolution SRμCT imaging

High-resolution 3D images of selected ROIs were acquired at the X-ray Tomographic Microscopy Station of the Materials Science beamline at the Swiss Light Source (SLS) (Stampanoni et al., 2002) using a local tomography setup described elsewhere (Heinzer et al., 2006). Briefly, the system was operated at 17.5 keV with a sample detector distance of 30 mm for distinct edge enhancement and an optical magnification resulting in isotropic voxels of nominal 1.4 μm. Each measurement included 1001 projections acquired at an integration time of 2 s each. Data were reconstructed using a filtered backprojection procedure. Due to relatively low signal to noise ratio and edge enhancement, segmentation was more involved than with the desktop μCT data, requiring two Gaussian filtration and segmentation passes on full and down-sampled image resolution, as well as component labeling to eliminate small pieces of noise. The net volume of the final images was 716×716×856 voxels, corresponding to 1.2 mm^3 of tissue volume.

Contouring and global morphometry

High-resolution images obtained from local SRμCT were contoured manually by two of the authors (G. K. and J. V.) to exclude vessels from outside the targeted anatomical ROI.

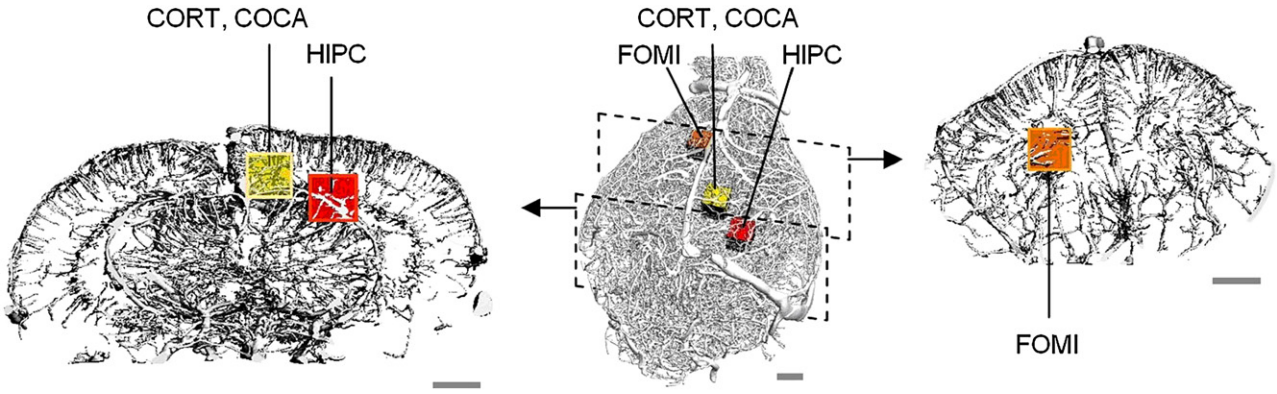

Fig. 1. Positioning of the regions of interest (ROI) in the mouse brain. The specific vascular architecture of different brain structures facilitated orientation. Shown are the ROIs selected for the present study in the corpus callosum (COCA), forceps minor (FOMI), cortex (CORT), and hippocampus (HIPC). Scale bars: 1 mm.

Contours were saved to disk as binary mask files for later use in morphometry and vascular network analysis. Direct 3D morphometry was performed for each high-resolution image using the software package IPL (Image Processing Language, Scanco Medical, Bassersdorf, Switzerland). This software was first developed to analyze μCT data obtained from bone biopsies, using 3D quantitative morphometry (Hildebrand et al., 1999; Odgaard and Gundersen, 1993; Parfitt et al., 1983). Assessed parameters include vessel volume per tissue volume (VV/TV), vessel thickness (V.Th), vessel separation (V.Sp), degree of anisotropy (DA), and specific vessel surface (VS/VV). Detailed descriptions of the morphometric parameters and their calculation are given elsewhere (Heinzer et al., 2006). Computations were performed on an OpenVMS cluster (HP, Palo Alto, USA). Due to the limited number of samples, rank–sum tests were performed to test for genotype differences within anatomical regions. Figures show the individual data points and indicate the median value per group. Both statistical testing and figure plotting were done using Matlab (The MathWorks Inc., Natick, MA, USA).

Vascular network analysis

Global morphometry offers robust quantification of complex structures. However it treats the input structure as one monolithic piece, missing vasculature-specific properties such as vessel bifurcations, individual vessel segments, or parent–child relations in the vessel hierarchy. We therefore designed an algorithm to decompose the complex vascular network into individual vessel segments suitable for quantitative analysis (Fig. 2). A segment was defined as a piece of vasculature connecting two vessel junctions (where vessel endpoints were considered as a case of trivial junctions), yielding a direct mapping of segments and junctions onto a mathematical graph (Bullitt et al., 1999). A graph in this context is defined as a tuple $<V, E>$, where V is a set of vertices and E a set of pairs of vertices. In a directed graph, the two vertices of an edge are ordered, the first vertex called the source, the second being the target. The degree of a vertex is defined as the number of edges associated with that vertex. A vascular network may now be represented as segment graph by associating each junction and

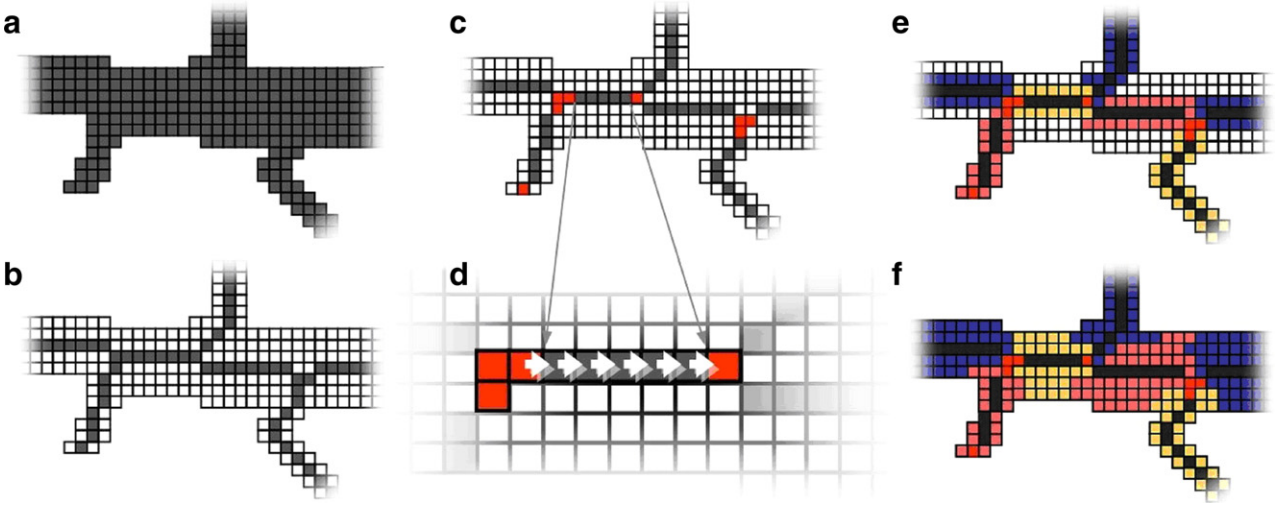

Fig. 2. Extraction of junctions and segments from binary image data. The original vascular structure (a) is thinned to its centerline (b). Voxels with one or more than 2 neighbors are marked in red as junction points (c). Segments are identified by following the centerline voxels from one junction to the next one (arrows, d). The vessel lumen is distributed on individual segments by layer-wise dilation starting at the centerline, with alternating segment order indicated by different colors (e, f).

each vessel dead end with a vertex and each segment with an edge in the graph.

Our network analysis algorithm operates in three major steps: (1) thinning of the binary input vasculature for centerline extraction using the efficient algorithm of Palagyi and Kuba (1998); (2) identification of junction points (vertices) and segment centerlines (edges); (3) quantification and statistical analysis of vessel segments and junctions. After image thinning (Figs. 2a, b), extraction of individual segments and attribution of length, diameter, and tortuosity for each segment were established as follows: (1) object voxels with 1 or more than 2 neighbors were marked as junction candidates (Fig. 2c); (2) neighboring junction candidates were grouped into one junction and stored as vertex of the segment graph; (3) for each junction and each segment start point the segment centerline was followed voxel by voxel until the next junction was reached (Fig. 2d). The segment along with the centerline was stored as new edge in the segment graph; (4) spurious leaf segments shorter than a user-defined minimum segment length were pruned, remaining segments were merged where appropriate. If this operation lead to degraded junctions (degree 0 or 2), they were deleted as well. (5) Neighboring junctions lying closer than a user-defined minimum junction distance are merged into one single bigger junction. The position of the adjacent segments remained unchanged. (6) Segments were dilated from centerlines back to the original volume one layer at a time, traversing the segment list back and forth, thus dividing the border zones equally between neighboring vessel (Figs. 2e, f).

In order to avoid image boundary artifacts, junctions lying within a border of four voxels from the image boundary as well as attached segments were excluded from statistical analysis. Tissue volume (TV) was calculated as the sum of voxels contained within both the four-voxel-border and the optionally user-supplied mask, multiplied by the volume of one voxel. Segment volume (S.V) was calculated as the total number of voxels associated with the segment, multiplied by the volume of one voxel (Fig. 2f). Vessel volume (VV) was then calculated as the sum of the volume of all vessels not touching the four-voxel-border. Segment length (S.L) was calculated along the segment centerline, including the center of source and target junctions (Fig. 2d). The segment thickness (S.Th) was estimated as the diameter of a regular cylinder of the given segment length and segment volume. Segment tortuosity (S.To) was calculated as the segment centerline divided by the minimum distance between source and target junctions. Thus, the minimal tortuosity is 1.0, corresponding to a perfectly straight segment. The junction degree (J.Deg) denotes the number of segments connected to a junction. Here, only true junctions were considered, neglecting trivial junctions, i.e. endpoints of leafs. Minimum junction degree is therefore 3. Segment density (S.N/TV) and junction density (J.N/TV) were calculated as the fraction of total number of segments and junctions per tissue volume, respectively. Apart from statistical analysis of network parameters over all segments, separate statistics were calculated for vessels with diameter <7.5 μm and vessels with diameter 7.5–30 μm.

The algorithm was implemented in modular, object-oriented fashion using the C++ programming language. Graph representation was facilitated using the graph template library (GTL, University of Passau, http://infosun.fmi.uni-passau.de/GTL/). Figure plotting and statistics were done analogous to the parameters from global morphometry.

Validation and performance of the vascular network analysis algorithm

In order to validate parameters obtained with the novel network analysis tool, TV, VV, and VV/TV also calculated with global morphometry were compared using linear regressions. For performance assessment, full network analysis including image reading, graph extraction, generation assignment, and statistical analysis was run on an Intel Itanium system with 16 GB RAM running OpenVMS (HP, Palo Alto, USA) and on an Intel Pentium 4 Mobile laptop computer (IBM, New York, USA) with a 2 GHz CPU and 1 GB RAM running Windows XP Professional.

Image quality control

In order to assess potential angiogenic sprouts (Patan, 2004) in our image data, we implemented two additional parameters in the network analysis software: leaf density (Lf.N/TV) indicates the relative number of segments with at least one junction of degree 1, i.e. which were only at one end connected to the vascular network. Free-hanging segment density (Fh.N/TV) indicated the relative number of segments that were completely disconnected from the vascular network. The related parameters leaf ratio (Lf.N/S.N) and free-hanging ratio (Fh.N/S.N) denoted the percentage of leafs and free-hanging segments per total segment number. In addition, 240 of such segments from one *tg* and one *wt* animal were manually classified as: (1) free-hanging, (2) disconnected leaf, defined as segments with an obvious interruption, i.e. after a gap of 5 to 20 μm the vessel continued, (3) potential angiogenic sprout, identified as dead end vessel where no continuing piece was visible.

Results

Characterization of vascular alterations in $VEGF_{165}$ tg mice

First we visualized the SRμCT image data followed by evaluation with global morphometry software to assess overall characteristics of the vasculature. The capillary network was visualized in high detail in all images (Fig. 3), as described earlier (Heinzer et al., 2006). Structural indices obtained from global morphometry (Fig. 4) revealed higher vessel volume density (VV/TV) in the gray matter (HIPC and CORT) in both mouse lines (Fig. 4a). In $VEGF_{165}$ tg mice the increased vessel volume density was found in the white matter structures (COCA and FOMI) although this observation reached statistical significance only for the FOMI. These findings confirmed our previous results (Vogel et al., 2004). Higher vessel volume density in tg mice was associated with a reduced vessel separation (V.Sp), an effect that was significant in both white matter structures (Fig. 4b). Investigation of vessel separation histograms indicated a shift towards smaller inter-vessel distances in the tg animals, with a distribution in the white matter similar to that of gray matter structures (Figs. 4d, e). Vessel thickness revealed no major differences between brain structures and mouse lines, confirming our previous findings of normal microvascular morphology in tg animals (Vogel et al., 2004) (Fig. 4c). The data obtained from global morphometry are summarized in the upper part of Table 1.

The same data were subsequently analyzed with our new network analysis software in order to evaluate additional segment and junction specific parameters missing in global morphometry

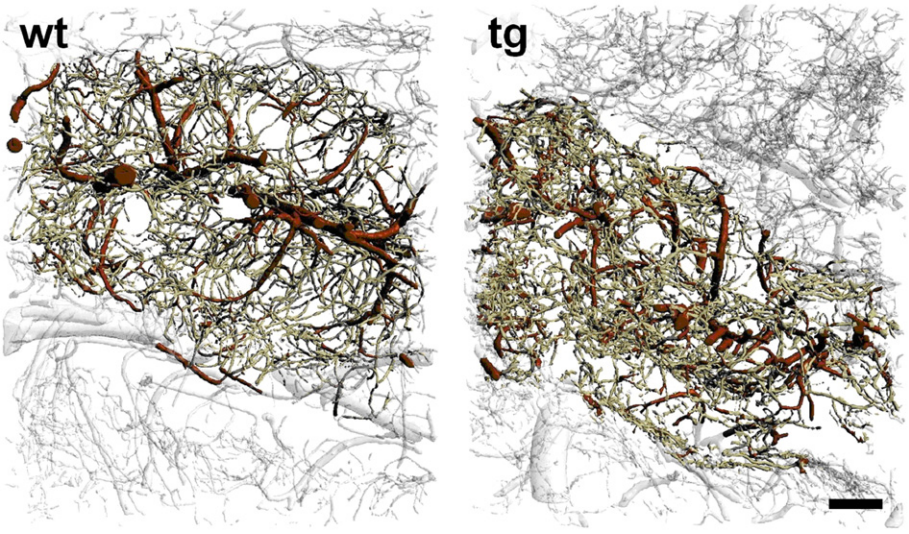

Fig. 3. Example of contoured vasculature in a sample of the hippocampus from a wt and a tg mouse. The higher vessel density in tg is evident. Semi-transparent vessels were lying outside the contour and thus were excluded from the analysis. Capillaries (<7.5 μm) are depicted in yellow and larger vessels (>7.5 μm) in red. Scale bar: 100 μm.

(Fig. 5). The threshold for capillary diameter was set to 7.5 μm, minimum leaf length to 30 μm, and minimum junction distance to 15 μm. Segment density was similarly increased in microvessels (<7.5 μm) and larger vessels (>7.5 μm) of the FOMI. In the other investigated white matter structure (COCA) comparable observations – although statistically not significant – could be made for both vessel size classes defined. Segment tortuosity in tg animals showed a slight trend to be increased for vessels <7.5 μm, but not

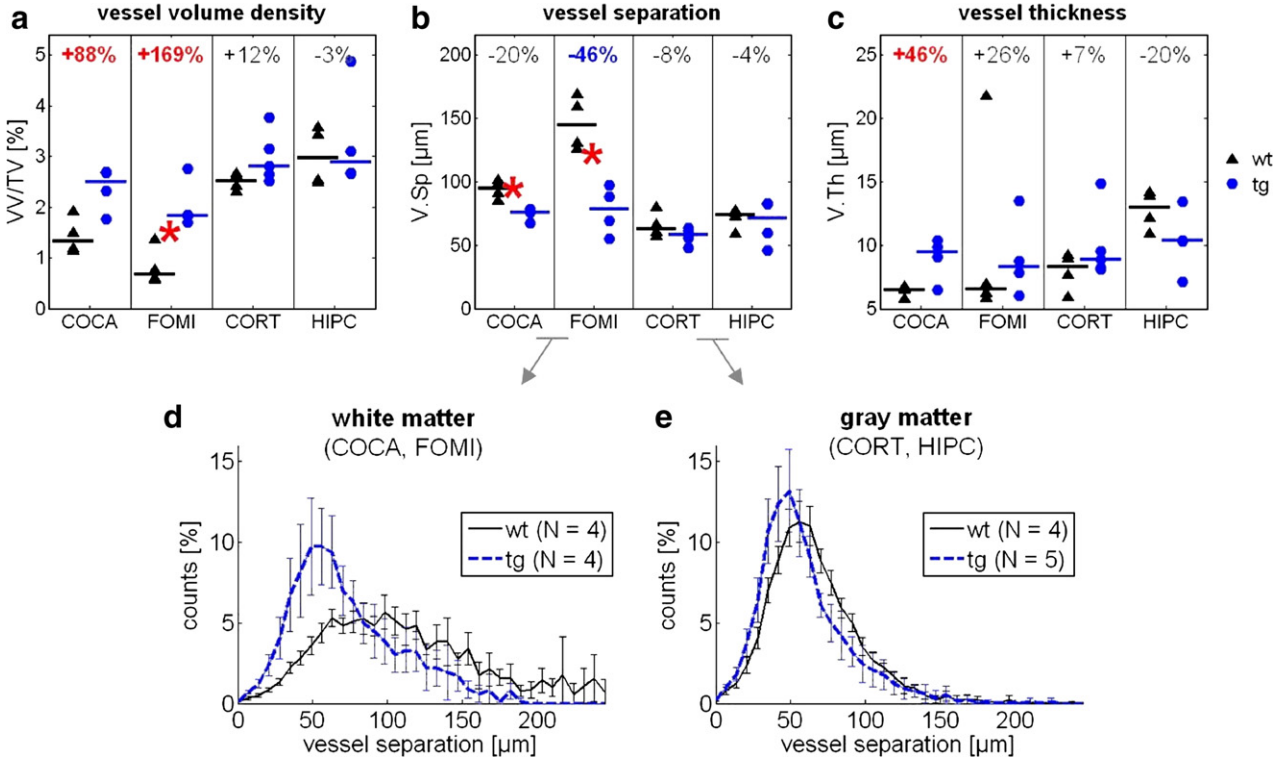

Fig. 4. Quantification of morphological alterations in $VEGF_{165}$ tg and control mice in the corpus callosum (COCA), forceps minor (FOMI), cortex (CORT), and hippocampus (HIPC), using global morphometry. The mean of each individual sample is shown as triangle (wt) or dot (tg) whereas the horizontal lines represent the median of all samples. Asterisks indicate significant differences based on a rank–sum test. In white matter structures of tg mice, vessel volume density (VV/TV, a) was increased and vessel separation (V.Sp, b) decreased when compared to wt controls. Vessel separation histograms (d, e) revealed a clear left shift in tg mice. Histograms of tg white matter structures appear similar to that of gray matter structures. Vessel thickness (V.Th, c) was marginally higher in white matter structures of tg mice.

Table 1
Morphometric parameters obtained from global morphometry (upper half) and vessel network analysis (lower half)

Procedure	Parameter	Unit	CORT		HIPC		COCA		FOMI	
			wt	tg	wt	tg	wt	tg	wt	tg
Global/tri	VV/TV	[%]	2.51	2.81	2.98	2.89	1.33	2.50	0.68	1.83
	VS/TV	[1/mm]	16.3	17.4	14.6	18.3	10.2	15.9	4.5	12.3
	VS/VV [1/mm]	[1/mm]	646	676	548	601	711	677	726	679
	dS/dr	[mm]	1493	2189	3089	2921	1361	2025	260	486
	DA	[1]	1.107	1.114	1.086	1.087	1.075	1.081	1.099	1.166
Global/dto	V.Th	[μm]	8.3	8.8	13.0	10.3	6.5	9.5	6.5	8.3
	V.Th.SD	[μm]	6.8	8.2	10.5	9.0	4.9	8.3	4.8	7.4
Global/dtb	V.Sp	[μm]	63.0	58.0	73.8	71.0	94.7	75.7	144.8	78.6
	V.Sp.SD	[μm]	24.8	24.2	31.6	32.6	38.6	35.3	62.2	31.5
Global/dtn	V.N	[1/mm]	15.7	17.2	13.4	14.3	10.5	13.1	6.9	12.8
Global/con	Conn.D	[1/mm^3]	10,462	6943	4772	9066	4849	5912	1143	2446
Trees/jnct	J.Deg	[1]	3.63	3.51	3.53	3.67	3.54	3.56	3.44	3.45
	J.Deg.SD	[1]	0.90	0.80	0.83	0.95	0.84	0.88	0.69	0.75
	Ep.N/TV	[1/mm^3]	1658	3812	3442	4609	2159	4517	866	3223
Trees/sgmt	VV/TV	[%]	1.88	2.31	2.40	2.80	0.95	2.12	0.43	1.16
	S.N/TV	[1/mm^3]	13,730	14,715	10,932	14,136	7299	12,763	2514	7414
	S.L	[μm]	53.0	56.0	60.5	56.0	63.0	58.0	59.5	58.5
	S.L.SD	[μm]	67.5	70.0	69.5	60.0	93.0	75.0	87.0	84.5
	S.Th	[μm]	5.6	5.5	5.8	6.0	5.3	5.9	5.3	5.5
	S.Th.SD	[μm]	27.2	29.3	31.3	31.1	8.5	31.6	8.7	9.3
	S.To	[1]	1.29	1.31	1.31	1.32	1.31	1.34	1.29	1.32

Parameters are grouped by anatomical ROI and genotype, indicating the median value of the 4–5 samples per group.

for larger vessels (Figs. 5c, d). Interestingly, vessel length (Fig. 5e) was identical for both genotypes in all brain structures investigated. Moreover, vessel length between white and gray matter structures was not different in wt mice despite the fact that their vessel volume density was higher in gray matter structures. To exclude hidden segment length changes smeared out by averaging, we also produced segment length histograms (data not shown). In contrast to vessel separation, these histograms were identical for both mouse lines in all investigated brain structures. Junction density (Fig. 5f) was slightly higher in tg mice in all brain structures, with a significant difference in the forceps minor (white matter). This effect was correlated with increased vessel volume density and increased segment density, also reflected by the fact that junction degree in white matter structures was not different between genotypes (Fig. 5g). The numbers from network analysis are summarized in the lower part of Table 1.

Validation and performance of the vascular network analysis algorithm

TV, VV, and VV/TV calculated with the novel network analysis tool as well as with global morphometry yielded very high correlation with an r^2 value of 0.99, 0.98, and 0.98, with *Y*-offsets of 0.02 mm^3, 0.00 mm^3, and 0.00%, respectively. With network analysis, TV was estimated 5.5% lower than with global morphometry, VV 17% lower, and VV/TV 15% lower, respectively. V.Th from global morphometry did not correlate with S.Th from network analysis ($r^2=0.34$), the latter giving values 90% lower than with global morphometry. This difference as well as the deviations in TV and VV is however expected (see Discussion). Connectivity density (Conn.D) partially correlated with J.N/TV and J.Deg ($r^2=0.66$ and $r^2=0.58$), reaching still higher correlation when taking the product of the network analysis parameters J.Deg * J.N/TV ($r^2=0.73$).

The performance characteristic of the proposed algorithm was assessed evaluating a vessel image at different cubic sub-volumes, ranging from 250 to 700 voxels side length. The number of junctions in the images ranged from 510 to 7441, that of segments from 651 to 11,148. Total execution time for the image of 250^3 voxels was 20 (28) s, for the image of 700^3 voxels 14.6 (24.8) min, where the first numbers indicate the values obtained on the Itanium system, and numbers in braces the values obtained on the Pentium 4 system. Average costs for the different parts of the analysis were, listed in descending order: graph extraction 90% (85%), statistical analysis 10% (12%), initialization 0.4% (1%), overhead 0.1% (2%), and generation assignment 0.01% (0.01%). Thus, almost all the computational time was consumed by graph extraction and statistics. Time for graph extraction was split on thinning 37% (65%), segment pruning 27% (11%), junction merging 22% (10%), segment extraction 8% (10%), and other less time consuming operations. These numbers apply to the image of 700^3 voxels, with shifted ratios for other image sizes: for small images, thinning takes up to 80% of the computational costs, while in larger images the network optimizations (segment pruning and junction merging) get more costly. Not surprisingly it turned out that execution time is dependent on the number of junctions and segments rather than on the actual image size. A linear regression of execution time with J.N for 12 samples of the same size with 7500 to 22,000 junctions yielded an r^2 of 0.89.

Image quality control

We finally assessed the number of leaf vessels present in our image data because they could represent angiogenetic sprouts (Patan, 2004) and thus important features of the angiogenic process. However, leafs could also be artifacts arising from the imaging process, in which case we wanted to know whether they differently affect VEGF tg and wt controls. Free-hanging segments

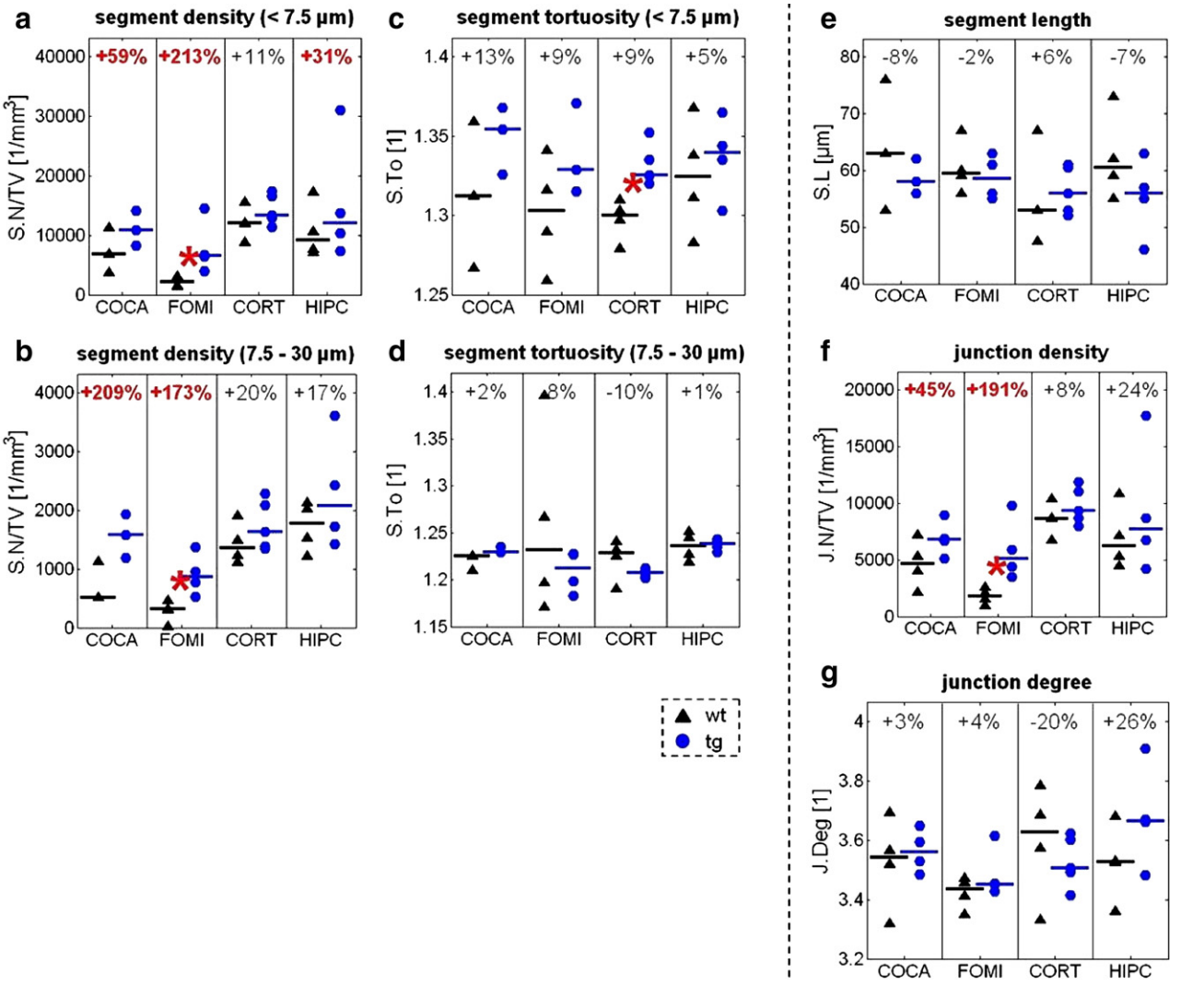

Fig. 5. Quantification of morphological alterations in $VEGF_{165}$ tg and control mice in the corpus callosum (COCA), forceps minor (FOMI), cortex (CORT) and hippocampus (HIPC), obtained from vascular network analysis. The mean of each individual sample is shown as triangle (wt) or dot (tg) whereas the horizontal lines represent the median of all samples. Asterisks indicate significant differences based on a rank–sum test. Segment density (S.N/TV, a, b) and segment tortuosity (S.To, c, d) are shown separately for vessels <7.5 µm and 7.5–30 µm (as shown in different colors for example for the hippocampus in Fig. 3). Segment density was mainly elevated in tg mice in white matter structures. Concerning the different size classes there was no clear difference in the increase in vessel density. Segment tortuosity was in tendency more increased in vessels <7.5 µm. Segment length (S.L, e) did not differ between both mouse lines. The higher junction density (J.N/TV, f) in tg mice was correlated with the increased segment density (S.N/TV, a, b). Junction degree (J.Deg, g) again was not different between both mouse lines.

surely indicate imaging artifacts. Median leaf ratio (Lf.N/S.N) for wt and tg animals respectively was 18%, 21% (COCA), 17%, 22% (FOMI), 11%, 15% (CORT), and 18%, 16% (HIPC) and median free-hanging ratio (Fh.N/S.N) for wt and tg animals respectively was 2.5%, 3.5% (COCA and FOMI), 0.8%, 2% (COCA), and 3%, 3% (HIPC). Both leaf and free-hanging ratio did not differ significantly between tg and wt animals.

Discussion

Therapeutic angiogenesis is believed to be highly beneficial for the treatment of ischemic diseases, although to date therapeutic growth induction of normal vessels is still not possible (Bruick and McKnight, 2001; Carmeliet, 2000). An earlier study in *human* $VEGF_{165}$ tg mice has shown that higher density of morphologically normal and perfused capillaries does not automatically lead to elevated blood flow capacity (Vogel et al., 2004). Our extended vessel analysis revealed that in tg mice length and tortuosity of microvessels are unchanged in brain structures with a significantly increased vessel volume density. This finding was unexpected since it argues against the postulated insertion of additional microvessels as bridges between existing capillaries and also against lengthening and subsequent coiling of preexisting capillaries (Detmar et al., 1998). Instead, our results imply that *human* $VEGF_{165}$ overexpression in the mouse brain forms complete additional micro-networks with apparently unchanged structural properties, but ineffectively inserted into the preexisting upstream arterial network.

Parameters calculated with the network analysis software correlate well with the values obtained from global morphometry

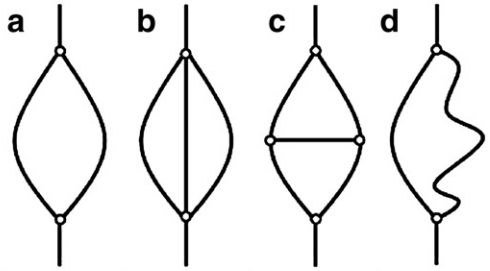

	a	b	c	d
J.N	2	2	4↑	2
J.Deg	3	4↑	3	3
S.N	4	5↑	7↑	4
S.L	normal	normal	short↓	long↑

Fig. 6. Schematic view of types of alterations in the microvasculature and their effect on important network parameters such as junction number (J.N), junction degree (J.Deg), segment number (S.N), and segment length (S.L). (a) Normal physiological pattern. (b, c) Insertion of redundant vessels. (d) Formation of elongated vessels. The table summarizes quantitative traits that can be calculated from analysis of the vessel graph.

(Table 1), indicating robust vessel quantification using the new tool. The fact that network analysis calculated vessel volume (VV) 17% lower than global morphometry primarily originates from vessel segments touching the image boundary, which were excluded from morphometric evaluation to avoid parameter distortion by truncated segments. Vessel volume is further reduced by branch pruning and the formation of junctions from several junction points. Tissue volume (TV) underestimation by 5% and the observed *Y*-offset of 0.02 mm^3 are as well explained by the exclusion of the border zone, leading in an image of $700^3/400^3$ voxels to a theoretical TV reduction of 3.4%/5.9% when compared to global morphometry. The very different values and the low correlation obtained for V.Th (global morphometry) and S.Th (network analysis) on the other hand are directly explained by the way the two parameters are calculated: global morphometry has no concept of segments and estimates the thickness of the entire vessel network by fitting spheres to the structure. Each voxel is attributed to the value of the largest enclosing sphere, and the average thickness is calculated as the average value of each voxel. A thick segment consisting of many voxels will have more weight in this averaging scheme than thin vessels containing only few voxels. Network analysis, on the other hand, has access to the thickness of each individual vessel, calculating the average as the mean thickness of all vessels (rather than over all voxels). Other parameters of the two morphometry schemes correlate partially, while J.Deg, S.N/TV etc. can only be obtained from network analysis since global morphometry completely lacks the concept of individual segments. Thus, network analysis complements global morphometry and has proven useful to reveal relevant vessel characteristics not accessible with global morphometry.

The ability of the new software to detect leaf vessels was helpful to identify imaging artifacts in the high-resolution image data. Transcriptional activity in the brains of tg and wt control mice is quite low and not different between both mouse lines (unpublished data), thus sprouting is probably not the only cause for the relatively high leaf ratio. Since an earlier study showed that all vessels in the brains of the $VEGF_{165}$ tg mice were perfused (Vogel et al., 2004), it is also unlikely that leaf vessels are caused by incomplete filling with casting resin. Free-hanging segments (about 3%) would have physically fallen out of the cast if incompletely filled. Such elements could be removed by a more aggressive component labeling. This in turn would result in an unwanted change of measures such as vessel separation or vessel volume density. Sources for imaging artifacts are low signal to noise ratio and suboptimal axis alignment in the tomographic experiments. Subsequent segmentation might thus be limited for proper reconstruction of all vessels. Nevertheless, images with even the highest leaf and free-hanging segment densities did not appear degraded by any means. Furthermore, leaf ratio and free-hanging segment ratio were not significantly different between wt and tg mice. Thus, leaf ratio and free-hanging segment ratio can serve as rigorous and very sensitive parameters for image quality.

Blood flow capacity through an organ primarily depends on the overall resistance of the vascular bed. The different previously proposed models to locally insert additional vessels segments into a capillary network are shown in Fig. 6, where (a) corresponds to the original network. An increased blood flow capacity is only possible when tubes are inserted as additional flow paths between in- and out-flow tract (b). Bridging between (c) or lengthening (d) of preexisting tubes would have either no effect or even reduce the blood flow capacity. The unchanged junction degree in $VEGF_{165}$ tg mice argues against the insertion of additional parallel vessel segments (b) in tg mice. With decreased segment length, the additionally observed increase in junction density and vessel volume density supports model (c). However, as segment length was found to be unchanged in tg mice we reject models (c) and (d). Thus the observed changes of network parameters match none of

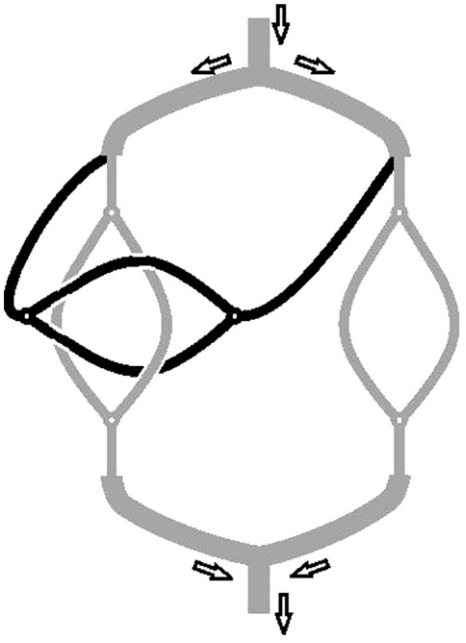

Fig. 7. Simplified model illustrating the insertion of an entire micro-network into the existing vasculature. In this case the additional micro-network (horizontal, black) is inserted as a bridge between upstream arteriols (gray) resulting in an increased junction number, unchanged junction degree, increased segment number, and unchanged segment length. This additional micro-network does not increase blood flow capacity of the whole vascular network. The direction of blood flow is indicated with arrows.

the proposed models, probably due to the fact that they are based on two dimensions and two vessel orders only. The observed vascular network parameters (increased VV.Dens, S.N/TV, and J.N/TV, unchanged S.L and J.Deg) suggest insertion of complete micro-networks into higher order vessel networks. A simplified model of such an insertion is shown in Fig. 7. This model implies that the "angiogenic quantum", i.e. the smallest vessel unit created as an endpoint during angiogenesis and subsequent remodeling in $VEGF_{165}$ tg mice, is a small micro-network rather than a single microvessel. Single capillaries generated during angiogenesis by sprouting or intussusception (Burri and Djonov, 2002; Pettersson et al., 2000) appear to be only a transient phenomenon. Interestingly segment length as well as junction degree is also similar in white and gray matter structures of wt animals, despite much higher vessel volume density in gray matter structures (Gobel et al., 1990) (Fig. 5). Whether the angiogenic quantum can be generalized to vasculature produced from endogenous VEGF remains subject to further investigations.

Several questions however remain unanswered: How many vessels compose the angiogenic quantum? At which vessel order is the angiogenic quantum inserted into the existing vessel structure? The insertion of additional capillary networks can only result in an increased blood flow capacity if in parallel the main feeding arteries increase their conductance, a process called arteriogenesis (Buschmann and Schaper, 1999; Scholz et al., 2001). It is known that information can be transferred from low order vessels upstream to higher order vessels (de Witt, 2004, 2000), a mechanism believed to be an essential part of the vascular remodeling process (Pries et al., 2001). Arteriogenesis in turn is dependent on a reduction of the downstream vascular resistance as it is mainly triggered by elevated wall shear stress (Schaper and Scholz, 2003). As long as remodeling of the vascular network downstream of a given artery does not result in decreased resistance, arteriogenesis will not be initiated. This suggests that remodeling of feeding arterioles and arteries is secondary to insertion of new vessel elements. In wt gray matter structures both angiogenesis and arteriogenesis are triggered by the high demand of nutrients and oxygen and lead to an increase in blood flow capacity. In tg animals however, where vascular density exceeds the blood flow demand, signals for the coordination of both processes are obviously missing.

The transgenic overexpression of VEGF in our mice is driven by the neuron-specific enolase promoter (Vogel et al., 2004) that directs VEGF overexpression to neurons that are located in gray matter structures. However VEGF overexpression had almost exclusively an effect in white matter structures. In white matter of tg mice despite six-fold VEGF overexpression vessel density increased and vessel separation decreased not to values higher or lower respectively than those of gray matter structures of wt animals. This suggests yet unknown mechanisms that define a maximum capillary density that cannot be exceeded despite continuous VEGF overexpression. Capillary density in white matter structures is normally below this limit, permitting a response to VEGF overexpression.

In conclusion, our results demonstrate that structural indices obtained from network analysis complement global morphometry and together provide new insight in the complex vessel network organization. Hierarchical high-resolution SRμCT imaging and the newly developed network analysis tool allowed precise characterization of the 3D microvascular network architecture in wt and $VEGF_{165}$ tg mice. Our results suggest that in our tg mice the smallest angiogenic quantum, i.e. the final, stable result of angiogenesis and subsequent remodeling, is not a single microvessel but rather a complete micro-network. Since cerebral perfusion in tg mice is not increased, these additional networks appear to be inserted ineffectively on a higher level of the network structure. The presented method is also applicable to other experimental settings and thus may significantly contribute to the understanding of vascular remodeling involved in health and disease.

Acknowledgments

This work was supported by the Stiftung für wissenschaftliche Forschung an der Universität Zürich to J.V. and the Swiss National Science Foundation (PP-104317/1). We thank Dr. Amela Groso from the Swiss Light Source (SLS, Paul Scherrer Institut, Villigen, Switzerland) for her support during the experiments.

References

Bruick, R.K., McKnight, S.L., 2001. Building better vasculature. Genes. Dev. 15, 2497–2502.

Bullitt, E., Aylward, S.R., Liu, A., Stone, J., Mukherji, S.K., Coffey, C., Gerig, G., Pizer, S.M., 1999. 3D graph description of the intracerebral vasculature from segmented MRA and tests of accuracy by comparison with X-ray angiograms. IPMI 1613, 308–321.

Bullitt, E., Muller, K.E., Jung, I., Lin, W., Aylward, S., 2005. Analyzing attributes of vessel populations. Med. Image Anal. 9, 39–49.

Burri, P.H., Djonov, V., 2002. Intussusceptive angiogenesis—the alternative to capillary sprouting. Mol. Aspects Med. 23, S1–S27.

Buschmann, I., Schaper, W., 1999. Arteriogenesis versus angiogenesis: two mechanisms of vessel growth. News Physiol. Sci. 14, 121–125.

Carmeliet, P., 2000. VEGF gene therapy: stimulating angiogenesis or angioma-genesis? Nat. Med. 6, 1102–1103.

Carmeliet, P., Jain, R.K., 2000. Angiogenesis in cancer and other diseases. Nature 407, 249–257.

de Witt, C., 2004. Connexins pave the way for vascular communication. News Physiol. Sci. 19, 148–153.

de Witt, C., Roos, F., Bolz, S.S., Kirchhoff, S., Kruger, O., Willecke, K., Pohl, U., 2000. Impaired conduction of vasodilation along arterioles in connexin40-deficient mice. Circ. Res. 86, 649–655.

Detmar, M., Brown, L.F., Schon, M.P., Elicker, B.M., Velasco, P., Richard, L., Fukumura, D., Monsky, W., Claffey, K.P., Jain, R.K., 1998. Increased microvascular density and enhanced leukocyte rolling and adhesion in the skin of VEGF transgenic mice. J. Invest. Dermatol. 111, 1–6.

Dorr, A., Sled, J.G., Kabani, N., 2007. Three-dimensional cerebral vasculature of the CBA mouse brain: a magnetic resonance imaging and micro computed tomography study. NeuroImage 35, 1409–1423.

Gobel, U., Theilen, H., Kuschinsky, W., 1990. Congruence of total and perfused capillary network in rat brains. Circ. Res. 66, 271–281.

Hayashi, T., Abe, K., Itoyama, Y., 1998. Reduction of ischemic damage by application of vascular endothelial growth factor in rat brain after transient ischemia. J. Cereb. Blood Flow Metab. 18, 887–895.

Heinzer, S., Krucker, T., Stampanoni, M., Abela, R., Meyer, E.P., Schuler, A., Schneider, P., Muller, R., 2006. Hierarchical microimaging for multiscale analysis of large vascular networks. NeuroImage 32, 626–636.

Hildebrand, T., Laib, A., Muller, R., Dequeker, J., Ruegsegger, P., 1999. Direct three-dimensional morphometric analysis of human cancellous bone: microstructural data from spine, femur, iliac crest, and calcaneus. J. Bone Miner. Res. 14, 1167–1174.

Iadecola, C., 2004. Neurovascular regulation in the normal brain and in Alzheimer's disease. Nat. Rev., Neurosci. 5, 347–360.

Isner, J.M., Pieczek, A., Schainfeld, R., Blair, R., Haley, L., Asahara, T., Rosenfield, K., Razvi, S., Walsh, K., Symes, J.F., 1996a. Clinical

evidence of angiogenesis after arterial gene transfer of phVEGF165 in patient with ischaemic limb. Lancet 348, 370–374.

Isner, J.M., Walsh, K., Symes, J., Pieczek, A., Takeshita, S., Lowry, J., Rosenfield, K., Weir, L., Brogi, E., Jurayj, D., 1996b. Arterial gene transfer for therapeutic angiogenesis in patients with peripheral artery disease. Hum. Gene Ther. 7, 959–988.

Kassab, G.S., 2006. Scaling laws of vascular trees: of form and function. Am J. Physiol.: Heart Circ. Physiol. 290, H894–H903.

Kiessling, F., Greschus, S., Lichy, M.P., Bock, M., Fink, C., Vosseler, S., Moll, J., Mueller, M.M., Fusenig, N.E., Traupe, H., Semmler, W., 2004. Volumetric computed tomography (VCT): a new technology for noninvasive, high-resolution monitoring of tumor angiogenesis. Nat. Med. 10, 1133–1138.

Krucker, T., Lang, A., Meyer, E.P., 2006. New polyurethane-based material for vascular corrosion casting with improved physical and imaging characteristics. Microsc. Res. Tech. 69, 138–147.

Marti, H.J., Bernaudin, M., Bellail, A., Schoch, H., Euler, M., Petit, E., Risau, W., 2000. Hypoxia-induced vascular endothelial growth factor expression precedes neovascularization after cerebral ischemia. Am. J. Pathol. 156, 965–976.

Marxen, M., Thornton, M.M., Chiarot, C.B., Klement, G., Koprivnikar, J., Sled, J.G., Henkelman, R.M., 2004. MicroCT scanner performance and considerations for vascular specimen imaging. Med. Phys. 31, 305–313.

Ment, L.R., Stewart, W.B., Fronc, R., Seashore, C., Mahooti, S., Scaramuzzino, D., Madri, J.A., 1997. Vascular endothelial growth factor mediates reactive angiogenesis in the postnatal developing brain. Brain Res. Dev. Brain Res. 100, 52–61.

Odgaard, A., Gundersen, H.J., 1993. Quantification of connectivity in cancellous bone, with special emphasis on 3-D reconstructions. Bone 14, 173–182.

Palagyi, K., Kuba, A., 1998. A 3D 6-subiteration thinning algorithm for extracting medical lines. Pattern Recogn. Lett. 19, 613–627.

Parfitt, A.M., Mathews, C.H., Villanueva, A.R., Kleerekoper, M., Frame, B., Rao, D.S., 1983. Relationships between surface, volume, and thickness of iliac trabecular bone in aging and in osteoporosis. Implications for the microanatomic and cellular mechanisms of bone loss. J. Clin. Invest. 72, 1396–1409.

Patan, S., 2004. Vasculogenesis and angiogenesis. Cancer Treat. Res. 117, 3–32.

Pettersson, A., Nagy, J.A., Brown, L.F., Sundberg, C., Morgan, E., Jungles, S., Carter, R., Krieger, J.E., Manseau, E.J., Harvey, V.S., Eckelhoefer, I.A., Feng, D., Dvorak, A.M., Mulligan, R.C., Dvorak, H.F., 2000. Heterogeneity of the angiogenic response induced in different normal adult tissues by vascular permeability factor/vascular endothelial growth factor. Lab. Invest. 80, 99–115.

Pries, A.R., Secomb, T.W., 2000. Microvascular adaptation—regulation, coordination and function. Z. Kardiol. 89 (Suppl. 9), 117–120.

Pries, A.R., Secomb, T.W., Gaehtgens, P., 1995a. Design principles of vascular beds. Circ. Res. 77, 1017–1023.

Pries, A.R., Secomb, T.W., Gaehtgens, P., 1995b. Structure and hemodynamics of microvascular networks: heterogeneity and correlations. Am J. Physiol.: Heart Circ. Physiol. 269, H1713–H1722.

Pries, A.R., Secomb, T.W., Gaehtgens, P., 1998. Structural adaptation and stability of microvascular networks: theory and simulations. Am. J. Physiol.: Heart Circ. Physiol. 275 (2), H349–H360.

Pries, A.R., Reglin, B., Secomb, T.W., 2001. Structural adaptation of microvascular networks: functional roles of adaptive responses. Am. J. Physiol.: Heart Circ. Physiol. 281, H1015–H1025.

Riew, C.K., Smith, R.W., 1971. Modified osmium tetroxide stain for microscopy of rubber-toughened resins. J. Polym. Sci. A, Poly. Chem. 9, 2739–2745.

Schaper, W., Scholz, D., 2003. Factors regulating arteriogenesis. Arterioscler. Thromb. Vasc. Biol. 23, 1143–1151.

Scholz, D., Cai, W.J., Schaper, W., 2001. Arteriogenesis, a new concept of vascular adaptation in occlusive disease. Angiogenesis 4, 247–257.

Stampanoni, M., Borchert, G., Wyss, P., Abela, R., Patterson, B., Hunt, S., Vermeulen, D., Ruegsegger, P., 2002. High resolution X-ray detector for synchrotron-based microtomography. Nucl. Instrum. Methods Phys. Res. 491, 292–301.

Vogel, J., Horner, C., Haller, C., Kuschinsky, W., 2003. Heterologous expression of human VEGF165 in rat brain: dose-dependent, heterogeneous effects on CBF in relation to vascular density and cross-sectional area. J. Cereb. Blood Flow Metab. 23, 423–431.

Vogel, J., Gehrig, M., Kuschinsky, W., Marti, H.H., 2004. Massive inborn angiogenesis in the brain scarcely raises cerebral blood flow. J. Cereb. Blood Flow Metab. 24, 849–859.

Wang, Y., Kilic, E., Kilic, U., Weber, B., Bassetti, C.L., Marti, H.H., Hermann, D.M., 2005. VEGF overexpression induces post-ischaemic neuroprotection, but facilitates haemodynamic steal phenomena. Brain 128, 52–63.

Zakrzewicz, A., Secomb, T.W., Pries, A.R., 2002. Angioadaptation: keeping the vascular system in shape. News Physiol. Sci. 17, 197–201.